ACS APPLIED MATERIALS & INTERFACES

One-Dimensional Rod-Like Sb_2S_3-Based Anode for High-Performance Sodium-Ion Batteries

Hongshuai Hou, Mingjun Jing, Zhaodong Huang, Yingchang Yang, Yan Zhang, Jun Chen, Zhibin Wu, and Xiaobo Ji*

College of Chemistry and Chemical Engineering, Central South University, Changsha 410083, China

Supporting Information

ABSTRACT: Due to the high theoretical capacity of 946 mAh g^{-1}, Sb_2S_3 can be employed as promising electrode material for sodium-ion batteries (SIBs). Herein, the sodium storage behaviors of one-dimensional (1D) Sb_2S_3-based materials (Sb_2S_3 and Sb_2S_3@C rods) are successfully studied for the first time, displaying good cyclability and rate capability owing to their unique morphology and structure. Specifically, the Sb_2S_3@C rods electrode presents greatly enhanced electrochemical properties, resulting from the introduction of thin carbon layers which can effectively alleviate the strain caused by the large volume change and simultaneously improve the conductivity of electrode during cycling. At a current density of 100 mA g^{-1}, it delivers a high capacity of 699.1 mAh g^{-1} after 100 cycles, which corresponds to 95.7% of the initial reversible capacity. Even at a high current density of 3200 mA g^{-1}, the capacity can still reach 429 mAh g^{-1}. This achievement may be a significant exploration for develpoing novel 1D Sb-based materials or metal sulfide SIBs anodes.

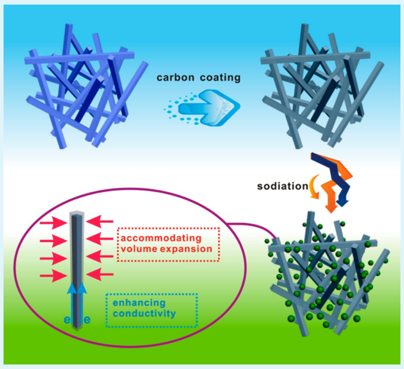

KEYWORDS: *Sb_2S_3, rod, anode, sodium-ion battery, electrochemistry*

1. INTRODUCTION

The development of sodium-ion batteries (SIBs) paralleled that of lithium-ion batteries (LIBs) through the 1980s. However, due to the lower electrochemical standard potential of Li^+/Li (−3.04 V vs SHE) and smaller size of Li^+, the LIBs with higher energy density played the dominant role in both research and commercial fields. Thus, the investigation and development of SIBs were largely depressed after the success of the commercial application of LIBs in the 1990s,[1] followed by the rapid development of portable electronics and electric vehicles market leading to the heavy demand of LIBs. Recently, more and more scientists are gradually beginning to realize that the limited lithium source reserve in the earth may hamper the power supply for large-scale application field,[2,3] which tells that exploring new alternative batteries becomes imperative. Just under such a background, SIBs catch the researchers' attention again and are becoming one of the hottest topics for emerging energy storage and conversion owing to the abundant reserves of sodium, which has similar physicochemical properties with lithium.[4] Nonetheless, several problems must be solved before such a battery can become a practical, commercial reality.[2] Research of SIBs is now in full swing to address these barriers and makes efforts to enable this emerging energy storage technology to become available in the coming years.

Currently, the negative electrode is one of the most troublesome components of SIBs since Na^+ ions cannot be intercalated to the typical graphitic carbons utilized in LIBs.[1] The discovery of suitable anode materials is a major challenge. Hence, the exploitation of excellent anode materials with high specific capacity, long cycle life and fast charge−discharge ability is highly desired.[5−7] In view of previous research reports,[8−13] Sb-based materials (Sb, Sb alloy and composite, Sb oxide and sulfide) might become one kind of quite available anode candidates for high-performance SIBs in considering their high theoretical capacities (Table 1). Since Qian et al.,[8] Xiao et al.[9], and Darwiche et al.[10] first reported the sodium storage properties of Sb/C, SnSb/C, and bulk Sb, respectively, in 2012, various metallic Sb anode materials have been studied, such as Sb/graphene,[14−16] Sb/carbon nanotubes,[17] Sb/carbon spheres,[18] Sb/carbon nanosheets,[19] Sb/carbon nanofibers,[20−23] pitaya-like Sb/carbon,[24] rod-like Sb/carbon composites,[25] SnSb,[26] Cu_2Sb,[27] Sb−Cu composite,[28] Zn_4Sb_3,[29] Mo_3Sb_7 alloy,[30] Sb nanocrystals,[31] and Sb hollow structures.[32,33] Whereas, although possessing higher theoretical specific capacity than that of metallic Sb, the research of antimony oxides and sulfides is so insufficient that only a few related works[11−13,34,35] are reported. Thus, it will be extremely meaningful to exploit novel antimony oxides or sulfides and explore their sodium storage behaviors.

Table 1. Maximum Theoretical Capacity of Sb-based Anode Materials for SIBs

	Sb	Sb_2S_3	Sb_2O_3	Sb_2O_4
maximum theoretical capacity (mAh g^{-1})	660	946	1109	1227

In the past few decades, metal sulfides have been considered as prominent candidates for LIBs resulting from their unique

Received: June 22, 2015
Accepted: August 18, 2015
Published: August 18, 2015

DOI: 10.1021/acsami.5b05509
ACS Appl. Mater. Interfaces 2015, 7, 19362−19369

physical and chemical properties including higher electrical conductivity, mechanical and thermal stability than those of their corresponding metal oxides, as well as their rich redox chemistry that contributes to the high specific capacity.[36] Similar to LIBs, metal sulfides can also be prospective anode materials for SIBs.[37,38] Antimony sulfide (Sb_2S_3) as anode material for LIBs has been extensively studied.[39−41] Recently, it has been confirmed that Sb_2S_3 can also be utilized as anode for SIBs.[13,35] Theoretically, Sb_2S_3 can undergo both conversion reaction and alloy formation, as described by eqs 1 and 2.[13]

$$\text{Conversion: } Sb_2S_3 + 6Na^+ + 6e^- \rightarrow 2Sb + 3Na_2S \qquad (1)$$

$$\text{Alloying: } 2Sb + 6Na^+ + 6e^- \rightarrow 2Na_3Sb \qquad (2)$$

It can be seen that 12 mol of electrons and Na ions are stored in one mole of Sb_2S_3, resulting in a high theoretical capacity of 946 mAh g^{-1}. Nevertheless, the practical is not perfect. Similar to LIBs, the rate of sodium insertion/extraction is hindered by the sluggish diffusivity of sodium ion in the bulk Sb_2S_3 and the low electrode/electrolyte contact surface of the bulk electrodes, resulting in low power. Additionally, a series of drawbacks deriving from the large volume change would occur during the sodiation/desodiation process, which can inevitably give rise to serious destruction of electrode structure, bringing about poor cycle life.[36] As suggested for conventional electrode materials for LIBs and SIBs, typically effective solution for the aforementioned issues mainly include preparing small-sized micro/nanostructure[42] and introducing carbon materials.[20,21,43]

It is noteworthy that one-dimensional (1D) micro/nanostructures have distinct chemical and electrical properties and greater chemical reactivity, which originate from their unique geometric characteristics, including ultrafine size effects, long-range orientation of the crystalline lattice, and the quantum confinement effects.[44] Naturally, 1D micro/nanostructures are expected to play important roles in nanotechnology and materials science, making them arrestive as active components for various applications.[45] When applied in batteries, they have been confirmed to be viable candidates with improved performances due to their peculiar properties, such as resistance to self-agglomeration, improved well-guided charge transfer kinetics and high specific surface area. Meanwhile, 1D micro/nanostructures can also allow for better accommodation of volume change during repeated charge−discharge process.[44]

In consideration of above-mentioned factors, in this study, we designed 1D Sb_2S_3-based materials to improve the electrochemical performances of SIBs. The obtained submicrosized rod-like Sb_2S_3 and Sb_2S_3@C composite through solvothermal method are first applied as anode materials for SIBs and exhibit good sodium storage properties. It is worthy to note that the rod-like Sb_2S_3@C composite with a uniform thin carbon layer displays much more outstanding electrochemical performance with superior cycle stability and remarkable rate capability.

2. EXPERIMENTAL SECTION

2.1. Materials. $SbCl_3$ and ethanol (Shanghai Titan Scientific Co., Ltd.); ethanediol, thiocarbamide, and glucose (Sinopharm Chemical Reagent Co., Ltd.); carboxymethyl cellulose (CMC) and $NaClO_4$ (Alfa Aesar); fluoroethylene carbonate (FEC), propylene carbonate and Na (Sigma-Aldrich).

2.2. Preparation of Sb_2S_3 Rods and Sb_2S_3@C rods. The Sb_2S_3 rods and Sb_2S_3@C rods were prepared through solvothermal method. Typically, 0.75 g thiocarbamide was dissolved in 60 mL ethanediol under magnetically stirring for 2 h. Next, the above-prepared solution was rapidly added into $SbCl_3$ solution (0.75 g $SbCl_3$ in 60 mL ethanediol) with continuous magnetic stirring for 4 h. Then, the mixed solution was transferred to a 150 mL stainless steel Teflon-lined autoclave, followed by being sealed and then heated inside a conventional oven at 180 °C for 12 h. Last, after the autoclave was naturally cooled to room temperature, a black precipitate was collected by centrifugation and was then washed thoroughly successively with anhydrous ethanol and deionized water. The collected precipitate was dried in vacuum at 80 °C overnight for later use. For the preparation of Sb_2S_3@C rods, $SbCl_3$ solution was replaced by the mixed solution of 0.75 g glucose and 0.75 g $SbCl_3$ in 60 mL ethanediol, and other conditions remained the same. The obtained products were further carbonized at 450 °C for 2 h under Ar atmosphere with a heating rate of 3 °C min^{-1}. Meanwhile, the prepared Sb_2S_3 rods were also calcined with the same condition.

2.3. Materials Characterization. Scanning electron microscope (SEM, FEI Quanta 200) equipped with energy dispersive spectrometer (EDS), transmission electron microscope (TEM, JEM-2100F), X-ray diffraction (XRD, Rigaku D/max 2550 VB+ 18 kW, Cu Kα radiation), and thermogravimetric analysis (TGA, NETZSCH STA449F3) were used to characterize the morphology and composition of the samples.

2.4. Electrochemical Measurements. Coin-type half-cells were assembled in a glovebox filled with Ar to investigate the sodium storage behaviors of as-prepared products. A homogeneous slurry was obtained through mixing the synthesized active materials with super P and carboxymethyl cellulose (70:15:15 in weight) in deionized water, and then it was painted on a copper foil. After solvent evaporation, the copper foil coated with active materials was cut, pressed, and further dried at 100 °C under vacuum for 12 h. The tailored Cu foil coated with active materials was utilized as work electrode, metallic sodium was employed as the counter electrode, and Celgard 2400 was used as the separator. The electrolyte was a solution of 1 M $NaClO_4$ in propylene carbonate (PC) with 5% fluoroethylene carbonate (FEC) additive. Cyclic voltammetric measurements were performed on Solartron Analytical to examine the cathodic and anodic reaction using the above-mentioned cell in the voltage range of 2.5−0.01 V (vs Na/Na^+) at a scan rate of 0.1 mV s^{-1}. Galvanostatic charge−discharge tests were carried out on Arbin battery cycler (BT2000) at suitable current densities between 0.01 and 2.5 V (vs Na/Na^+) for both charge (Na extraction) and discharge (Na insertion) at room temperature. The electrochemical impedance measurements were performed on Solartron Analytical at an AC voltage of 5 mV amplitude in the range of 100 kHz to 0.01 Hz after five charge−discharge cycles. The mass loading of the active material is about 0.8−1.0 mg. The specific capacity was calculated based on the weight of active materials (Sb_2S_3 or Sb_2S_3@C) only.

3. RESULTS AND DISCUSSION

3.1. Morphology, Structure, and Composition Analyses. The chemical composition and crystal structure are detected through XRD analysis. The XRD results of prepared samples are presented in Figure 1, and all the diffraction peaks of Sb_2S_3 and Sb_2S_3@C can be indexed to the standard card data of orthorhombic stibnite (JCPDS 42-1393). No other impurity

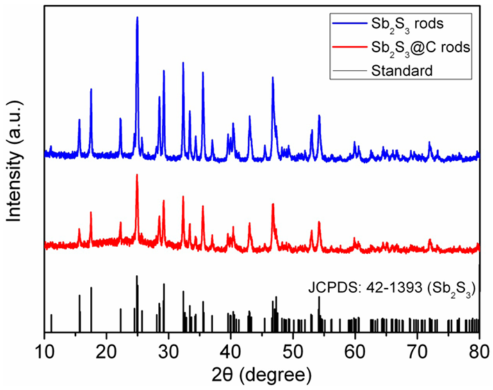

Figure 1. XRD patterns of Sb_2S_3 and Sb_2S_3@C rods.

peaks are observed, suggesting the obtained Sb_2S_3 is in high purity. The absence of carbon diffraction peaks in patterns of Sb_2S_3@C may be attributed to the amorphous structure and low content of carbon. It should be noted that some weaker peaks of stibnite in the pattern of Sb_2S_3@C disappeared because of the influences of surface carbon.

The morphology of as-prepared samples is expressed by SEM and TEM. Figure 2a−c shows SEM images of Sb_2S_3 with different magnification, and it is clear that Sb_2S_3 rods are stacked together, forming a haystack-like structure, and display well-defined rod-like structure. From the magnified SEM image (Figure 2c inset), it can be seen the Sb_2S_3 is cuboid rod. The haystack-like architecture can provide enlarged electrode/electrolyte contact area, leading to a large number of active sites for the following charge transfer reaction. In addition, the Na^+ ions diffusion paths are shortened, which can result in better kinetic conditions for the electrode material. The TEM image in Figure 2d indicates the solid rod-like morphology of Sb_2S_3, which agrees well with SEM results. The clear lattice fringe with an interplanar distance of 0.36 nm corresponding to the crystal plane of Sb_2S_3 (JCPDS 42-1393) can be observed in the high-resolution TEM (HRTEM) image (Figure 2e). The selected area electron diffraction (SAED, Figure 2f) result suggests the monocrystalline nature of Sb_2S_3 rods. The EDS spectra in Figure 2g reveal that the atomic ratio of Sb and S is quite close to 2:3, which further confirm that the resulted product is Sb_2S_3.

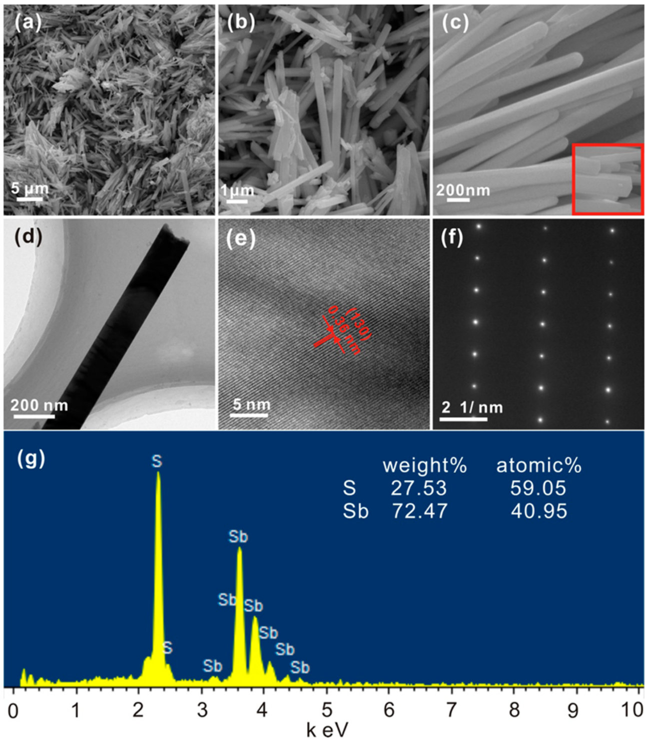

Figure 2. (a−c) SEM, (d) TEM, and (e) HRTEM images and (f) SAED and (g) EDS of Sb_2S_3 rods.

Figure 3a−c gives SEM images with different magnification of Sb_2S_3@C. After the coating of carbon was applied, one can see that the obtained products preserve the rod-shaped morphology and haystack-like architecture in a large area. The TEM image in Figure 3d further demonstrates the rod-shaped morphology and the amplified TEM images (Figure 3 e and f) clearly reveal that the rod's exterior is covered with a thin carbon layer, a typical core−shell structure was observed. Figure 3 g and h depict the contrast of Sb_2S_3 and Sb_2S_3@C rods, the difference is so clear due to the presence of carbon coating layer. Figure S1 displays the images of elemental mappings of S, Sb, and C; it is obvious that these three elements are uniformly distributed in the sample.

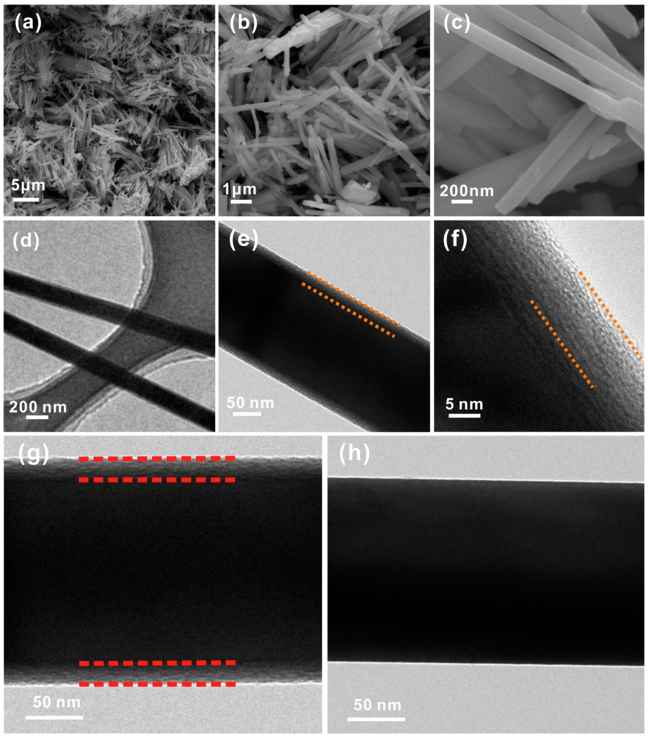

Figure 3. (a−c) SEM and (d−g) TEM images of Sb_2S_3@C rods and (h) TEM image of Sb_2S_3 rods.

In further experiments, TGA is carried out to evaluate the content of carbon in the Sb_2S_3@C composite. Figure 4a displays the TGA results of bare Sb_2S_3 rods and Sb_2S_3@C rods under air atmosphere. The weight loss can be observed for both bare Sb_2S_3 rods and Sb_2S_3@C rods, which can be ascribed to the conversion of Sb_2S_3 into Sb_2O_4 (confirmed by XRD in Figure 4b) during the burning process in air. Of course, the weight loss of Sb_2S_3@C is larger owing to the release of gas resulting from the combustion of carbon. According to TGA results, the calculated carbon content is ∼13%. The XRD patterns of combustion products of Sb_2S_3 rods and Sb_2S_3@C rods are displayed in Figure 4b, all diffraction peaks are in good agreement with orthorhombic Sb_2O_4 (JCPDS 71-0143), which confirms that the final products are Sb_2O_4 and this can assist TGA to calculate the carbon content.

On the basis of some previous laudable works,[46−48] the possible formation process of the Sb_2S_3 rods is depicted in Scheme 1. When the thiourea solution was added into the $SbCl_3$ solution, a Sb-thiourea complex was formed. During the heating process of solvothermal treatment, the chelation of Sb-thiourea would be weakened and Sb^{3+} would be released gradually. Meanwhile, thiourea would be broken and S^{2-} anions would be slowly released. And then amorphous orange-red $(Sb_2S_3)_n$ particles can be formed, resulting from the reaction of Sb^{3+} and S^{2-}. Under the solvothermal condition with high-temperature and high-pressure, the amorphous Sb_2S_3 particles nucleated and grew into small crystal in the solution. As reported, the unusual chain structure of Sb_2S_3 can facilitate the anisotropic growth of

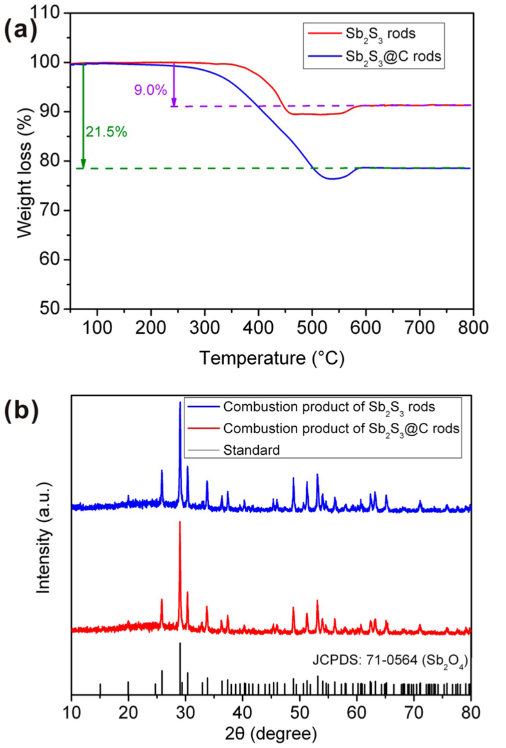

Figure 4. (a) TGA curves of Sb_2S_3 and Sb_2S_3@C rods and (b) XRD patterns of their combustion products.

Scheme 1. Schematic Illustration of the Formation Process of Sb_2S_3 Rod

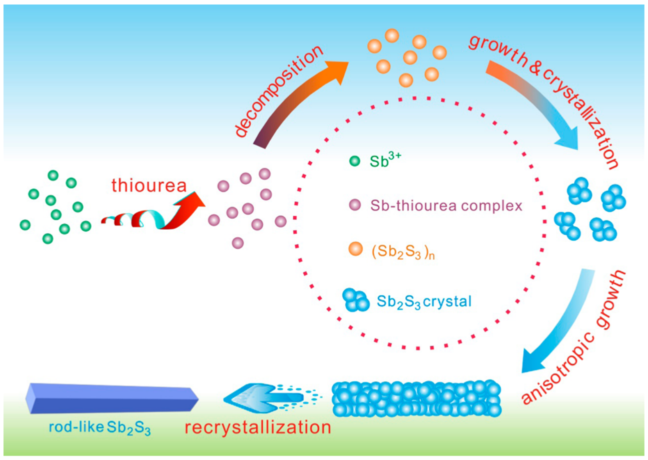

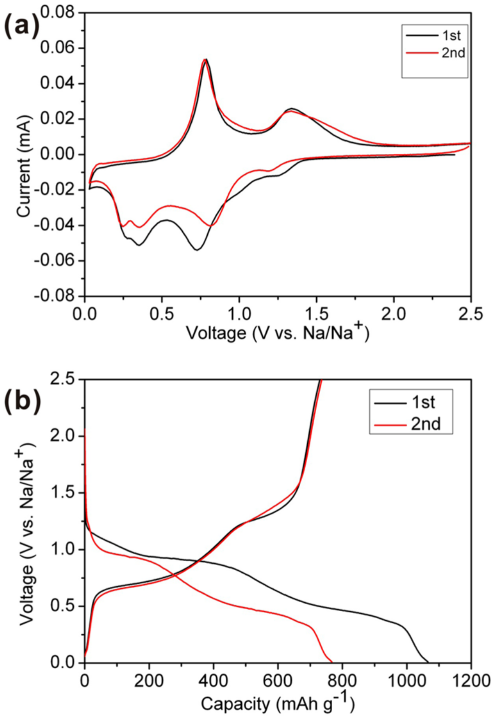

Figure 5. (a) Cyclic voltammograms and (b) charge−discharge profiles of Sb_2S_3@C rods.

Sb_2S_3 particles. In addition, under the direction of ethanediol solvent molecules, the collision of interparticles resulted in the formation of orientated connections along certain crystal face. With the prolongation of solvothermal treatment time, the orientated aggregations of Sb_2S_3 by self-assembling can further coalesce together by recrystallization and form 1D rod-like structure.

3.2. Sodium Storage Behaviors. Figure 5a shows typical cyclic voltammograms (CVs) of the half-cell at a scan rate of 0.1 mV s^{-1} between 0.01 and 2.5 V versus Na/Na^+ for the first two cycles. From the CV curves of Sb_2S_3@C rods, four peaks centered at around 1.30 V, 0.77 V, 0.35 V, 0.27 V are observed in the cathodic process, which are attributed to conversion reaction with sulfur atoms[13] ($Sb_2S_3 + 6\,Na^+ + 6\,e^- \rightarrow 2Sb + 3\,Na_2S$) and the alloying reaction of Sb with Na[8,49] ($2Sb + 6\,Na^+ + 6\,e^- \rightarrow 2\,Na_3Sb$). The broad peak from 0.50 to 1.10 V may contain the formation reaction of solid electrolyte interface (SEI) layer.[35] The anodic peaks centered at 0.77 and 1.35 V are related to the dealloying reaction[8,49] ($2\,Na_3Sb \rightarrow 2Sb + 6\,Na^+ + 6\,e^-$) and the formation of Sb_2S_3[13,35]($2Sb + 3\,Na_2S \rightarrow Sb_2S_3 + 6\,Na^+ + 6\,e^-$). As seen in the second cathodic scan, the location of peaks is slightly drifted, which probably can be ascribed to the formation of SEI layer and other irreversible side reactions in the first cycle.[35] After repeated sodiation−desodiation processes, the Sb_2S_3 is transformed from crystal phase to amorphous phase (Figure S2). The CV curves of Sb_2S_3 rods in Figure S3 are similar to those of Sb_2S_3@C rods. Figure 5b displays the charge−discharge profiles of Sb_2S_3@C rods electrode within a cutoff voltage window of 0.01−2.5 V versus Na^+/Na at a current density of 100 mA g^{-1}. The voltage profiles are typical characteristics of a Sb_2S_3@C electrode.[13,35] Specially, all the specific capacity values of Sb_2S_3@C rods reported in this paper are calculated on the basis of the total mass of Sb_2S_3/C composite. The first discharge delivers a capacity of 1066.0 mAh g^{-1}; however, upon recharging, only 730.3 mAh g^{-1} is obtained, giving a low Coulombic efficiency of 68.5%. This probably could be ascribed to the irreversible SEI phenomenon, which can be inferred from the difference of discharge profiles between the first and subsequent cycles.[35] Two plateaus can be observed in the discharge curve, the plateaus from 1.0 to 0.85 V and from 0.75 to 0.20 V correspond to the conversion reaction (peak at 1.3 V of CVs) and alloying reaction (peaks at 0.77 V, 0.35, and 0.27 V of CVs), respectively. The results of CVs and charge−discharge plateaus are in conformity with previous reports.[13,35] In addition, as displayed in Figure S3, the Sb_2S_3 rods electrode shows similar charge−discharge profiles as Sb_2S_3@C rods. There are two clear plateaus in the charge profile of Sb_2S_3@C electrode as well, the plateau between 0.62 and 0.85 V can be related to the peak centered at 0.77 V of CVs and the plateau from 1.2 to 1.6 V corresponds to the peak at 1.3 V of CVs.

Cycle stability of electrode material is naturally a most important parameter for its applicability. The cycle performances

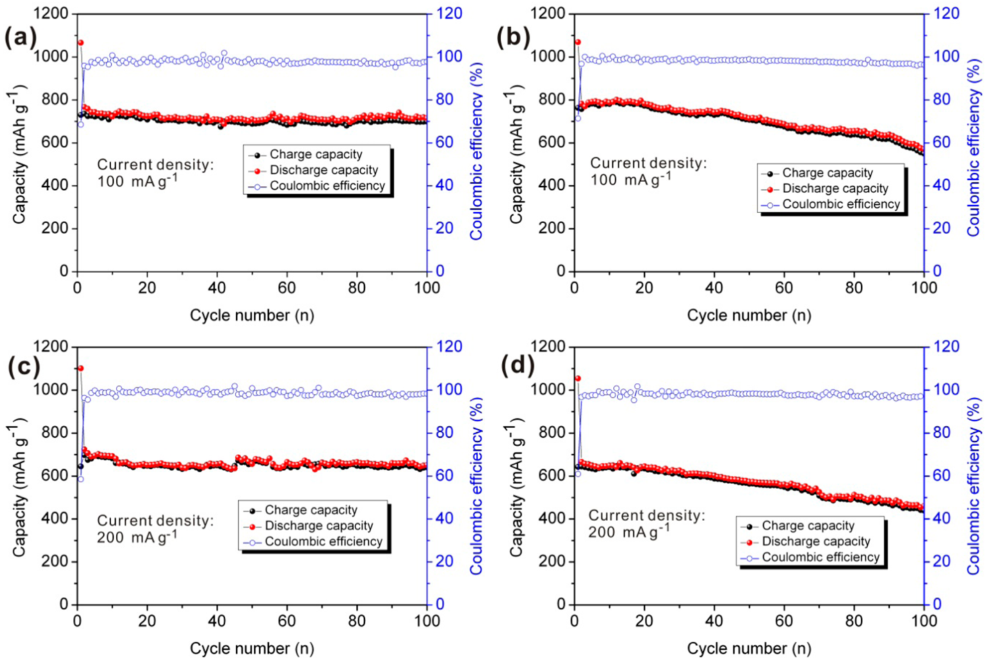

Figure 6. Cycle performances of (a, c) Sb_2S_3@C rods and (b, d) Sb_2S_3 rods.

of Sb_2S_3@C rods (Figure 6a,c) and Sb_2S_3 rods (Figure 6b,d) anodes were measured in the potential range of 0.01−2.5 V versus Na/Na$^+$ under constant current densities of 100 and 200 mA g^{-1}. Remarkably, the Sb_2S_3@C electrode shows a very stable cyclability, after 100 cycles, it still delivers a reversible capacity of 699.1 mAh g^{-1}, which corresponds to 95.7% of the initial reversible capacity, demonstrating the robustness of Sb_2S_3@C rods. For Sb_2S_3 rods, the capacity is stable for the initial 20 cycles but afterward drops gradually, and a residual capacity of 550.2 mAh g^{-1} with capacity retention of 72.1% remains after 100 cycles. At a high current density of 200 mA g^{-1}, the Sb_2S_3@C rods can still display prominent cycle stability with capacity retention of 99.3% after 100 cycles and the Sb_2S_3 rods only exhibit 68.3%. The initial cycle stability of Sb_2S_3 rods may be attributed to the 1D microstructure and haystack-like architecture. During repeated sodiation−desodiation processes, the structure was gradually destroyed by the huge volume change of particles, resulting in gradual capacity fading. Compared to the Sb_2S_3 rods electrode, the carbon layer on the surface of Sb_2S_3@C rods can act as a buffer to accommodate the volume expansion of active materials and preserve the structural integrity of electrode on cycling. As depicted in Figure S4, the rod-like structure can still be observed after cycling, suggesting the excellent structural stability of Sb_2S_3@C rods. On the basis of the above-mentioned results, the Sb_2S_3@C rods show much better cycle stability than that of Sb_2S_3 rods due to the introduction of carbon coating layer, agreeing well with reported carbon coating electrode materials for LIBs and SIBs.[50−52]

The rate performances of the Sb_2S_3 rods and Sb_2S_3@C rods electrodes at different current densities were further studied (Figure 7). As expected, the Sb_2S_3@C rods electrode displays superior rate capability compared with that of Sb_2S_3 rods. When cycled at current densities of 100, 200, 400, 800, 1600, and 3200 mA g^{-1}, the capacities of Sb_2S_3@C rods are around 724, 695, 680, 642, 578, and 429 mAh g^{-1}, respectively. When the current density is reduced back to 100 mA g^{-1}, the reversible capacity can recover to 635 mAh g^{-1}. Notably, even at a high current density of 3200 mA g^{-1}, the reversible capacity reaches 429 mAh g^{-1}, which is still higher than theoretical capacity of commercial graphite. In the same way, the reversible capacities of Sb_2S_3 rods at current densities of 100, 200, 400, 800, 1600, and 3200 mA g^{-1} are around 779, 674, 610, 556, 440, and 220 mA g^{-1}. The initial reversible capacities of Sb_2S_3@C rods and Sb_2S_3 rods are as high as 724 and 779 mAh g^{-1}, respectively, at a low current density of 100 mAh g^{-1}. Nevertheless, as the current densities increase, the capacity gap between Sb_2S_3 rods and Sb_2S_3@C rods is also enlarged (Figure S5). Obviously, far better rate performance of Sb_2S_3@C rods is observed, especially at higher current density, which may be attributed to the enhanced conductivity by the coated carbon layer.[50] Figure 7c,d presents the charge−discharge profiles of Sb_2S_3@C rods and Sb_2S_3 rods at different current densities. It can be seen that the overpotentials of sodiation/desodiation are increasing with the enhancement of current densities, and this issue is more serious for Sb_2S_3 rods electrode. Because the Coulombic efficiencies are quite close to 100% at high current densities, the major cause of reduced capacities should be the incomplete sodiation deriving from increasing overpotentials during discharge process.[23]

To further explore the better performance of the Sb_2S_3@C rods than that of Sb_2S_3 rods, we investigated the electrochemical impedance spectroscopy (EIS), and the EIS results are shown in Figure S6. Each of the two impedance spectra is composed of a depressed semicircle in the high-to-medium-frequency region, and a slope in the low-frequency region. The semicircle in the high-to-medium frequency region of the Nyquist plots is assigned to the SEI film resistance (R_{SEI}) and charge-transfer resistance (R_{ct}) between electrode and electrolyte, whereas the line inclined at ∼45° is the Warburg region associated with sodium-ion diffusion in the electrode.[53] As expected, the Sb_2S_3@C rods electrode exhibits a smaller semicircle diameter, indicating a lower interface impedance ($R_{int} = R_{SEI} + R_{ct}$). The inset in Figure S6 is the equivalent circuit model for the EIS studies. The Sb_2S_3 rods electrode displayed interface impedance (R_{int}) of 996 Ω, whereas the Sb_2S_3@C rods showed only 387.8 Ω, which is less than the

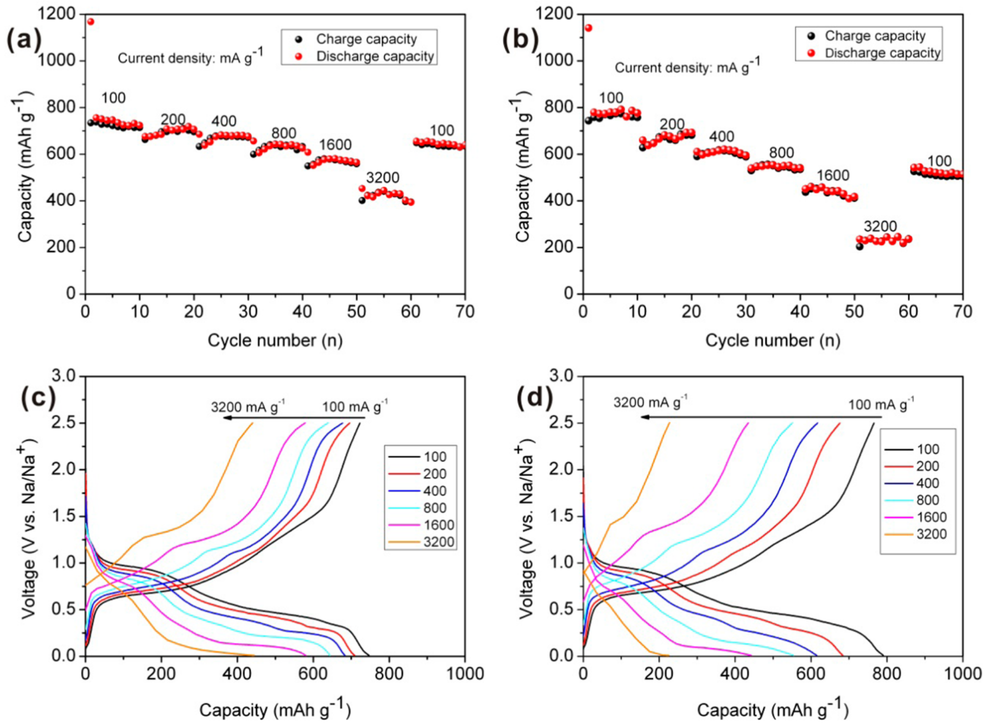

Figure 7. Rate performances and charge−discharge curves of (a and c) Sb_2S_3@C rods and (b and d) Sb_2S_3 rods.

Sb_2S_3 rods electrodes. The enhanced conductivity of Sb_2S_3@C rods is ascribed to the introduction of conductive carbon layer, which results in the improved electrochemical performances of Sb_2S_3@C rods.

Table S1 displays the comparison of the Sb_2S_3@C rods and reported Sb_2S_3-based anode materials. It can be seen that the electrochemical performances of Sb_2S_3@C are superior or comparable to those of recent Sb_2S_3-based anode materials in the literatures.

The excellent electrochemical performances of Sb_2S_3@C rods could be attributed to its unique structure and morphology. As shown in Scheme 2, the proposed mechanism of superior electrochemical performances is schematically illustrated: (1) the haystack-like architecture can offer short pathways for Na^+ diffusion, large specific space to facilitate the fast transfer of Na^+, and the facile electrolyte infiltration throughout the electrode; (2) the high aspect ratio of the rod provides a high reversible capacity by increasing the surface-to-volume ratio and reducing the Na diffusion distances; (3) the thin carbon layer coated on the Sb_2S_3 rods can be served as buffer to accommodate the volume change caused by repeated sodiation and desodiation during the cycling test; (4) additionally, the carbon layer can also be utilized as conductive medium which can facilitate the charge transport.

Scheme 2. Schematic Illustration of the Sb_2S_3 and Sb_2S_3@C Rods and the Sodiation of Sb_2S_3@C Rods

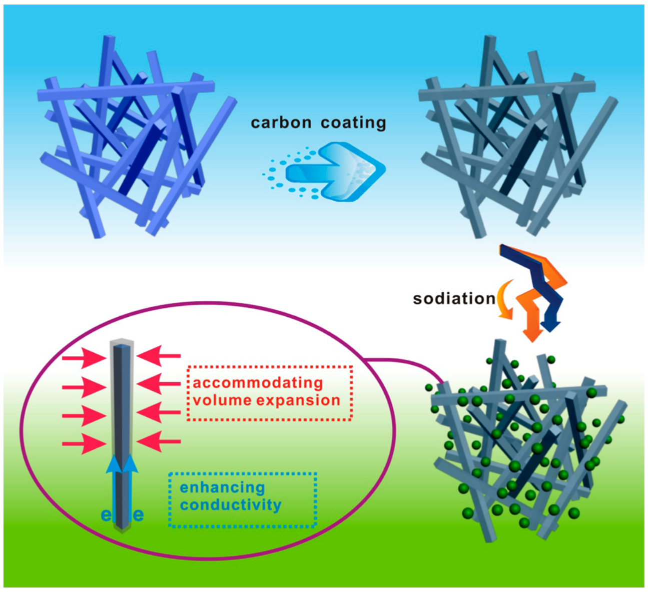

4. CONCLUSIONS

In summary, the well-defined Sb_2S_3 and Sb_2S_3@C rods exhibit enhanced sodium storage properties, which could be attributed to their unique morphology and structure. Numerous spaces among rods in the haystack-like architecture composed of random stacked rods can provide a large number of active sites for the charge transfer reaction and the diffusion length of electrons and ions can be effectively reduced; all these merits would contribute to the electrochemical performance of the electrode materials. Because the core−shell structure of Sb_2S_3@C and ultrathin carbon layers can effectively alleviate the strain caused by the large volume change and improve the conductivity of electrode during cycling, the Sb_2S_3@C rods electrode shows much more remarkable cycle stability and rate capability. Cycling at a current density of 100 mA g^{-1}, the electrode depicts a quite high capacity of 699.1 mAh g^{-1} after 100 cycles, corresponding to capacity retention of 95.7%. And a high capacity of 429 mAh g^{-1} is still observed at a current density of 3200 mA g^{-1}. Therefore, it is our anticipation that 1D Sb_2S_3-based materials will be readily applied in next-generation SIBs, and this achievement can be extened to other 1D Sb-based or metal sulfide electrode materials for SIBs.

■ ASSOCIATED CONTENT

Supporting Information

The Supporting Information is available free of charge on the ACS Publications website at DOI: 10.1021/acsami.5b05509.

> Cyclic voltammograms and charge−discharge curves of Sb_2S_3 rods, rate capability of Sb_2S_3@C rods and Sb_2S_3 rods and electrochemical impedance spectra (EIS) of Sb_2S_3 and Sb_2S_3@C rods, SEM and XRD of Sb_2S_3@C electrode after cycling. (PDF)

■ AUTHOR INFORMATION

Corresponding Author

* E-mail: xji@csu.edu.cn. Tel: +86 731-88879616. Fax: +86 731-88879616.

Notes

The authors declare no competing financial interest.

■ ACKNOWLEDGMENTS

This work was financially supported by the National Natural Science Foundation of China (21473258), Program for the New Century Excellent Talents in University (NCET-11-0513), Distinguished Young Scientists of Hunan Province (13JJ1004), the Hunan Provincial Innovation Foundation for Postgraduate (CX2015B039), Natural Science Foundation of Hunan (2014GK2016), and the State Key Laboratory of Powder Metallurgy, Central South University, Changsha, China.

■ REFERENCES

(1) Kundu, D.; Talaie, E.; Duffort, V.; Nazar, L. F. The Emerging Chemistry of Sodium Ion Batteries for Electrochemical Energy Storage. *Angew. Chem., Int. Ed.* **2015**, *54*, 3431−3448.

(2) Palomares, V.; Serras, P.; Villaluenga, I.; Hueso, K. B.; Carretero-González, J.; Rojo, T. Na-Ion Batteries, Recent Advances and Present Challenges to Become Low Cost Energy Storage Systems. *Energy Environ. Sci.* **2012**, *5*, 5884−5901.

(3) Slater, M. D.; Kim, D.; Lee, E.; Johnson, C. S. Sodium-Ion Batteries. *Adv. Funct. Mater.* **2013**, *23*, 947−958.

(4) Yabuuchi, N.; Kubota, K.; Dahbi, M.; Komaba, S. Research Development on Sodium-Ion Batteries. *Chem. Rev.* **2014**, *114*, 11636−11682.

(5) Dahbi, M.; Yabuuchi, N.; Kubota, K.; Tokiwa, K.; Komaba, S. Negative Electrodes for Na-Ion Batteries. *Phys. Chem. Chem. Phys.* **2014**, *16*, 15007−15028.

(6) Kim, Y.; Ha, K. H.; Oh, S. M.; Lee, K. T. High-Capacity Anode Materials for Sodium-Ion Batteries. *Chem. - Eur. J.* **2014**, *20*, 11980−11992.

(7) Kim, S. W.; Seo, D. H.; Ma, X.; Ceder, G.; Kang, K. Electrode Materials for Rechargeable Sodium-Ion Batteries: Potential Alternatives to Current Lithium-Ion Batteries. *Adv. Energy Mater.* **2012**, *2*, 710−721.

(8) Qian, J.; Chen, Y.; Wu, L.; Cao, Y.; Ai, X.; Yang, H. High Capacity Na-Storage and Superior Cyclability of Nanocomposite Sb/C Anode for Na-Ion Batteries. *Chem. Commun.* **2012**, *48*, 7070−7072.

(9) Xiao, L.; Cao, Y.; Xiao, J.; Wang, W.; Kovarik, L.; Nie, Z.; Liu, J. High Capacity, Reversible Alloying Reactions in SnSb/C Nanocomposites for Na-Ion Battery Applications. *Chem. Commun.* **2012**, *48*, 3321−3323.

(10) Darwiche, A.; Marino, C.; Sougrati, M. T.; Fraisse, B.; Stievano, L.; Monconduit, L. Better Cycling Performances of Bulk Sb in Na-Ion Batteries Compared to Li-Ion Systems: An Unexpected Electrochemical Mechanism. *J. Am. Chem. Soc.* **2012**, *134*, 20805−20811.

(11) Sun, Q.; Ren, Q.-Q.; Li, H.; Fu, Z.-W. High Capacity Sb_2O_4 Thin Film Electrodes for Rechargeable Sodium Battery. *Electrochem. Commun.* **2011**, *13*, 1462−1464.

(12) Hu, M.; Jiang, Y.; Sun, W.; Wang, H.; Jin, C.; Yan, M. Reversible Conversion-Alloying of Sb_2O_3 as a High-Capacity, High-Rate, and Durable Anode for Sodium Ion Batteries. *ACS Appl. Mater. Interfaces* **2014**, *6*, 19449−19455.

(13) Yu, D. Y. W.; Prikhodchenko, P. V.; Mason, C. W.; Batabyal, S. K.; Gun, J.; Sladkevich, S.; Medvedev, A. G.; Lev, O. High-Capacity Antimony Sulphide Nanoparticle-Decorated Graphene Composite as Anode for Sodium-Ion Batteries. *Nat. Commun.* **2013**, *4*, 2922−2928.

(14) Zhang, Y.; Xie, J.; Zhu, T.; Cao, G.; Zhao, X.; Zhang, S. Activation of Electrochemical Lithium and Sodium Storage of Nanocrystalline Antimony by Anchoring on Graphene via a Facile In-Situ Solvothermal Route. *J. Power Sources* **2014**, *247*, 204−212.

(15) Nithya, C.; Gopukumar, S. rGO/nano Sb Composite: a High Performance Anode Material for Na^+ Ion Batteries and Evidence for the Formation of Nanoribbons from the Nano rGO Sheet During Galvanostatic Cycling. *J. Mater. Chem. A* **2014**, *2*, 10516−10525.

(16) Zhang, W.; Liu, Y.; Chen, C.; Li, Z.; Huang, Y.; Hu, X. Flexible and Binder-Free Electrodes of Sb/rGO and $Na_3V_2(PO_4)_3$/rGO Nanocomposites for Sodium-Ion Batteries. *Small* **2015**, *11*, 3822.

(17) Zhou, X.; Dai, Z.; Bao, J.; Guo, Y.-G. Wet Milled Synthesis of an Sb/MWCNT Nanocomposite for Improved Sodium Storage. *J. Mater. Chem. A* **2013**, *1*, 13727−13731.

(18) Ko, Y. N.; Kang, Y. C. Electrochemical Properties of Ultrafine Sb Nanocrystals Embedded in Carbon Microspheres for Use as Na-ion Battery Anode Materials. *Chem. Commun.* **2014**, *50*, 12322−12324.

(19) Zhou, X.; Zhong, Y.; Yang, M.; Hu, M.; Wei, J.; Zhou, Z. Sb Nanoparticles Decorated N-Rich Carbon Nanosheets as Anode Materials for Sodium Ion Batteries with Superior Rate Capability and Long Cycling Stability. *Chem. Commun.* **2014**, *50*, 12888−12891.

(20) Zhu, Y.; Han, X.; Xu, Y.; Liu, Y.; Zheng, S.; Xu, K.; Hu, L.; Wang, C. Electrospun Sb/C Fibers for a Stable and Fast Sodium-Ion Battery Anode. *ACS Nano* **2013**, *7*, 6378−6386.

(21) Wu, L.; Hu, X.; Qian, J.; Pei, F.; Wu, F.; Mao, R.; Ai, X.; Yang, H.; Cao, Y. Sb−C Nanofibers with Long Cycle Life as an Anode Material for High-Performance Sodium-Ion Batteries. *Energy Environ. Sci.* **2014**, *7*, 323−328.

(22) Hou, H.; Jing, M.; Yang, Y.; Zhang, Y.; Song, W.; Yang, X.; Chen, J.; Chen, Q.; Ji, X. Antimony Nanoparticles Anchored on Interconnected Carbon Nanofibers Networks as Advanced Anode Material for Sodium-Ion Batteries. *J. Power Sources* **2015**, *284*, 227−235.

(23) Nam, D.-H.; Hong, K.-S.; Lim, S.-J.; Kim, M.-J.; Kwon, H.-S. High-Performance Sb/Sb_2O_3 Anode Materials Using a Polypyrrole Nanowire Network for Na-Ion Batteries. *Small* **2015**, *11*, 2885.

(24) Wu, L.; Lu, H.; Xiao, L.; Ai, X.; Yang, H.; Cao, Y. Electrochemical Properties and Morphological Evolution of Pitaya-Like Sb@C Microspheres as High-Performance Anode for Sodium ion Batteries. *J. Mater. Chem. A* **2015**, *3*, 5708−5713.

(25) Fan, L.; Zhang, J.; Cui, J.; Zhu, Y.; Liang, J.; Wang, L.; Qian, Y. Electrochemical Performance of Rod-Like Sb-C Composite as Anodes for Li-Ion and Na-Ion Batteries. *J. Mater. Chem. A* **2015**, *3*, 3276−3280.

(26) He, M.; Walter, M.; Kravchyk, K. V.; Erni, R.; Widmer, R.; Kovalenko, M. Monodisperse SnSb Nanocrystals for Li-ion and Na-ion Battery Anodes: Synergy and Dissonance Between Sn and Sb. *Nanoscale* **2015**, *7*, 455−459.

(27) Baggetto, L.; Carroll, K. J.; Hah, H.-Y.; Johnson, C. E.; Mullins, D. R.; Unocic, R. R.; Johnson, J. A.; Meng, Y. S.; Veith, G. M. Probing the Mechanism of Sodium Ion Insertion into Copper Antimony Cu_2Sb Anodes. *J. Phys. Chem. C* **2014**, *118*, 7856−7864.

(28) Lin, Y.-M.; Abel, P. R.; Gupta, A.; Goodenough, J. B.; Heller, A.; Mullins, C. B. Sn−Cu Nanocomposite Anodes for Rechargeable Sodium-Ion Batteries. *ACS Appl. Mater. Interfaces* **2013**, *5*, 8273−8277.

(29) Jackson, E. D.; Green, S.; Prieto, A. L. Electrochemical Performance of Electrodeposited Zn_4Sb_3 Films for Sodium-Ion Secondary Battery Anodes. *ACS Appl. Mater. Interfaces* **2015**, *7*, 7447−7450.

(30) Baggetto, L.; Allcorn, E.; Unocic, R. R.; Manthiram, A.; Veith, G. M. Mo_3Sb_7 as a Very Fast Anode Material for Lithium-Ion and Sodium-Ion Batteries. *J. Mater. Chem. A* **2013**, *1*, 11163−11169.

(31) He, M.; Kravchyk, K.; Walter, M.; Kovalenko, M. V. Monodisperse Antimony Nanocrystals for High-Rate Li-ion and Na-ion Battery Anodes: Nano versus Bulk. *Nano Lett.* **2014**, *14*, 1255−1262.

(32) Hou, H.; Jing, M.; Yang, Y.; Zhu, Y.; Fang, L.; Song, W.; Pan, C.; Yang, X.; Ji, X. Sodium/Lithium Storage Behavior of Antimony Hollow Nanospheres for Rechargeable Batteries. *ACS Appl. Mater. Interfaces* **2014**, *6*, 16189−16196.

(33) Hou, H.; Jing, M.; Yang, Y.; Zhang, Y.; Zhu, Y.; Song, W.; Yang, X.; Ji, X. Sb Porous Hollow Microspheres as Advanced Anode Materials for Sodium-Ion Batteries. *J. Mater. Chem. A* **2015**, *3*, 2971−2977.

(34) Zhou, X.; Liu, X.; Xu, Y.; Liu, Y.; Dai, Z.; Bao, J. An SbO_x/Reduced Graphene Oxide Composite as a High-Rate Anode Material for Sodium-Ion Batteries. *J. Phys. Chem. C* **2014**, *118*, 23527−23534.

(35) Zhu, Y.; Nie, P.; Shen, L.; Dong, S.; Sheng, Q.; Li, H.; Luo, H.; Zhang, X. High Rate Capability and Superior Cycle Stability of a Flower-Like Sb_2S_3 Anode for High-Capacity Sodium Ion Batteries. *Nanoscale* **2015**, *7*, 3309−3315.

(36) Rui, X.; Tan, H.; Yan, Q. Nanostructured Metal Sulfides for Energy Storage. *Nanoscale* **2014**, *6*, 9889−9924.

(37) Hu, Z.; Wang, L.; Zhang, K.; Wang, J.; Cheng, F.; Tao, Z.; Chen, J. MoS_2 Nanoflowers with Expanded Interlayers as High-Performance Anodes for Sodium-Ion Batteries. *Angew. Chem., Int. Ed.* **2014**, *53*, 12794−12798.

(38) Hu, Z.; Zhu, Z.; Cheng, F.; Zhang, K.; Wang, J.; Chen, C.; Chen, J. Pyrite FeS_2 for High-Rate and Long-Life Rechargeable Sodium Batteries. *Energy Environ. Sci.* **2015**, *8*, 1309−1316.

(39) Yu, D. Y. W.; Hoster, H. E.; Batabyal, S. K. Bulk Antimony Sulfide with Excellent Cycle Stability as Next-Generation Anode for Lithium-Ion Batteries. *Sci. Rep.* **2014**, *4*, 4562−4567.

(40) Prikhodchenko, P. V.; Gun, J.; Sladkevich, S.; Mikhaylov, A. A.; Lev, O.; Tay, Y. Y.; Batabyal, S. K.; Yu, D. Y. W. Conversion of Hydroperoxoantimonate Coated Graphenes to Sb_2S_3@Graphene for a Superior Lithium Battery Anode. *Chem. Mater.* **2012**, *24*, 4750−4757.

(41) Park, C.-M.; Hwa, Y.; Sung, N.-E.; Sohn, H.-J. Stibnite (Sb_2S_3) and Its Amorphous Composite as Dual Electrodes for Rechargeable Lithium Batteries. *J. Mater. Chem.* **2010**, *20*, 1097−1102.

(42) Zhang, Q.; Uchaker, E.; Candelaria, S. L.; Cao, G. Nanomaterials for Energy Conversion and Storage. *Chem. Soc. Rev.* **2013**, *42*, 3127−3171.

(43) Ko, Y. N.; Park, S. B.; Kang, Y. C. Design and Fabrication of New Nanostructured SnO_2-Carbon Composite Microspheres for Fast and Stable Lithium Storage Performance. *Small* **2014**, *10*, 3240−3245.

(44) Jiang, J.; Li, Y.; Liu, J.; Huang, X. Building One-Dimensional Oxide Nanostructure Arrays on Conductive Metal Substrates for Lithium-Ion Battery Anodes. *Nanoscale* **2011**, *3*, 45−58.

(45) Tian, J.; Zhao, Z.; Kumar, A.; Boughton, R. I.; Liu, H. Recent Progress in Design, Synthesis, and Applications of One-Dimensional TiO_2 Nanostructured Surface Heterostructures: a Review. *Chem. Soc. Rev.* **2014**, *43*, 6920−6937.

(46) Zhu, Q.-A.; Gong, M.; Zhang, C.; Yong, G.-b.; Xiang, S. Preparation of Sb_2S_3 Nanomaterials with Different Morphologies via a Refluxing Approach. *J. Cryst. Growth* **2009**, *311*, 3651−3655.

(47) Zhu, G. Q.; Liu, P.; Miao, H. Y.; Zhu, J. P.; Bian, X. B.; Liu, Y.; Chen, B.; Wang, X. B. Large-Scale Synthesis of Ultralong Sb_2S_3 Sub-Microwires via a Hydrothermal Process. *Mater. Res. Bull.* **2008**, *43*, 2636−2642.

(48) Geng, Z. R.; Wang, M. X.; Yue, G. H.; Yan, P. X. Growth of Single-Crystal Sb_2S_3 Nanowires via Solvothermal Route. *J. Cryst. Growth* **2008**, *310*, 341−344.

(49) Baggetto, L.; Ganesh, P.; Sun, C.-N.; Meisner, R. A.; Zawodzinski, T. A.; Veith, G. M. Intrinsic Thermodynamic and Kinetic Properties of Sb Electrodes for Li-Ion and Na-Ion Batteries: Experiment and Theory. *J. Mater. Chem. A* **2013**, *1*, 7985−7994.

(50) Liang, J.; Yu, X.-Y.; Zhou, H.; Wu, H. B.; Ding, S.; Lou, X. W. Bowl-like SnO_2@Carbon Hollow Particles as an Advanced Anode Material for Lithium-Ion Batteries. *Angew. Chem., Int. Ed.* **2014**, *53*, 12803−12807.

(51) Wang, J.; Luo, C.; Gao, T.; Langrock, A.; Mignerey, A. C.; Wang, C. An Advanced MoS_2/Carbon Anode for High-Performance Sodium-Ion Batteries. *Small* **2015**, *11*, 473−481.

(52) Ge, Y.; Jiang, H.; Zhu, J.; Lu, Y.; Chen, C.; Hu, Y.; Qiu, Y.; Zhang, X. High Cyclability of Carbon-Coated TiO_2 Nanoparticles as Anode for Sodium-Ion Batteries. *Electrochim. Acta* **2015**, *157*, 142−148.

(53) Zhu, Y.; Wen, Y.; Fan, X.; Gao, T.; Han, F.; Luo, C.; Liou, S.-C.; Wang, C. Red Phosphorus Single-Walled Carbon Nanotube Composite as a Superior Anode for Sodium Ion Batteries. *ACS Nano* **2015**, *9*, 3254−3264.